

Photothermal catalytic CO₂ oxidative dehydrogenation of propane over a dual functional Pt-GaN/SrTiO₃ catalyst

Sen-Wang Wang^a, Zhen-Hong He^{a,*}, Yue Tian^a, Zhan-Jun Zhu^a, Yong-Chang Sun^a, Kuan Wang^a, Weitao Wang^a, Yang Yang^a, Huan Wang^a, Zhao-Tie Liu^{a,b,**}

^a Shaanxi Key Laboratory of Chemical Additives for Industry, College of Chemistry and Chemical Engineering, Shaanxi University of Science and Technology, Xi'an 710021, China

^b School of Chemistry & Chemical Engineering, Shaanxi Normal University, Xi'an 710119, China



ARTICLE INFO

Keywords:

Photothermal catalysis
Oxidative dehydrogenation of propane
CO₂
Dual-functional catalysts
Reverse water-gas shift reaction

ABSTRACT

Photothermal CO₂ oxidative dehydrogenation of propane (CO₂-ODHP) is an environmentally friendly and sustainable route for propylene production and CO₂ utilization. In the present work, we developed a Pt-GaN/SrTiO₃ dual-functional catalyst to facilitate the reaction. The catalyst achieved propylene and CO yields of 1 mmol·g_{cat}⁻¹·h⁻¹ and 1.2 mmol·g_{cat}⁻¹·h⁻¹ under photothermal conditions at 320 °C, surpassing the performance of previously reported catalysts. Additionally, control experiments and *in situ* DRIFTS analyses corroborated that GaN and Pt were primarily responsible for the activation of C–H and C=O bonds, respectively, and the photothermal route worked via a distinguished intermediate for CO₂ activation in contrast to the thermal route. DFT calculations supported the reaction route involving the coupling direct dehydrogenation of propane and reverse water-gas shift reaction. The present work shines a light on the design of photothermal catalysts with dual functions, particularly for the activation of CO₂ and light hydrocarbons. Additionally, it proposes a strategy to initiate high-temperature reactions at relatively lower temperatures.

1. Introduction

With a great increase in the demand for downstream products such as polypropylene, the efficient synthesis of propylene is significantly important [1]. Conventional synthesis methods involve steam cracking (SC) and fluid catalytic cracking (FCC) of naphtha, heavy oil, etc. [2], which produce low selectivity to propylene since it is the by-product of ethylene. These routes, however, still cause a significant gap in propylene production [3]. Recently, the dehydrogenation of propane, as an on-purpose route, is particularly interesting especially upon the success of shale gas exploitation. CO₂ oxidative dehydrogenation of propane (CO₂-ODHP), not only produces propylene from propane but also utilizes the waste CO₂ resource, which is a “one stone two birds” route under the background of carbon neutrality.

In recent years, the CO₂-ODHP has made great progress although the reaction is still in challenging and rarely applied in industry. An array of efficient catalysts were developed, including metal oxides with polyvalent states and oxygen storage/release capacity (CrO_x, Ga₂O₃, MoO₃,

CeO₂, Fe₂O₃, In₂O₃, etc.) via Mars-van Krevelen (MvK) mechanism [4–11], or a combination of precious and non-precious metals (Pt, Ru, Pd, Co, Zn, and Ni) via the coupled reactions of direct dehydrogenation of propane (DDHP) and reverse water gas shift (RWGS) [3,12–16]. Together with these catalysts, in our group, GaN/zeolite catalysts were established and showed acceptable performances in CO₂-ODHP [17–20]. The active sites were found to be Si-O-GaN-H species, which achieves the C–H activation and CO₂ reduction. These findings greatly promote the development of CO₂-ODHP. However, all the above-mentioned catalysts worked at high temperatures, typically greater than 500 °C. The high temperature causes the formation of deposited carbon and aggregation of the active site, and low selectivity to propylene. Additionally, CO₂-ODHP is an endothermic reaction, and low temperature is unfavorable. This contradiction is difficult to reconcile in conventional thermal catalysis. To overcome this challenge, our group has, for the first time, introduced light into the reaction, tapping into the synergistic advantages of both light and thermal to achieve the CO₂-ODHP at a lower temperature such as 300 °C [21–23]. The synergistic effect

* Corresponding author.

** Corresponding author at: School of Chemistry & Chemical Engineering, Shaanxi Normal University, Xi'an 710119, China.

E-mail addresses: hezhenhong@sust.edu.cn (Z.-H. He), ztliu@snnu.edu.cn (Z.-T. Liu).

between light and thermal conditions could greatly promote the catalytic performances over the BiOI-based catalysts[21,22]. We found that the oxygen vacancy (O_v) on BiOI can reduce CO_2 to CO, while the lattice oxygen (O_{lat}) relative to the oxidative dehydrogenation of propane to propylene. In addition, VO_x - and Bi-based catalysts were reported to be active for photothermal propane dehydrogenation (Table S1), and for comparison, the recently reported thermal catalysts were also collected in Table S2. Typically, the photothermal route operates at relatively low temperatures, while the thermal route is conducted at high temperatures.

Based on our recent findings, GaN has demonstrated the ability to activate C=O and C-H bonds, making it a promising catalyst especially in CO_2 -ODHP[20,24]. Furthermore, GaN is a wide-gap semiconductor material, which possesses a bandgap energy of 3.4 eV at room temperature. It has been widely applied in photo-emitting device applications; however, it could be relatively less used alone in photocatalysis[25], particularly for its wide bandgap energy, which mainly applies in the UV region[26], resulting in low catalytic activity. To extend the adsorption band to visible light, many approaches were adopted, including morphological control[26], metal oxide binding [27], heteroatom doping[28], etc. These successes in photocatalysis bring the light in further applications of GaN-based catalysts for their unique properties.

In this work, we established a combination of GaN and metal oxide catalyst for the photothermal CO_2 -ODHP. Among various tested photocatalytic active metal oxides, $SrTiO_3$ (STO), as a perovskite material, showed the best performances for its special photoelectronic properties, abundant oxygen content, and excellent thermal stability[29,30]. Taking consideration of that Pt-based catalysts are highly active for C-H and CO_2 activations, in this study, a one-step method combining wet impregnation and *in situ* nitridation was employed to load Pt and GaN onto STO substrates. Additionally, introduction of Pt species, which are highly efficient in utilizing the solar spectrum and activating CO_2 , greatly improves the performance of photothermal CO_2 hydrogenation [31,32]. A series of spectroscopic studies provided strong evidence for the generation of O_v , reduction in band gap, and excellent photoelectric characteristics of STO induced by the incorporation of Pt and GaN. Furthermore, experiments data and *in situ* DRIFTS analyses validated the primary roles of Pt and GaN in the catalytic process. Different intermediates involved in CO_2 conversion were identified in the thermal and photothermal CO_2 -ODHP reactions. The findings from *in situ* DRIFTS experiments and DFT calculations demonstrated that the photothermal CO_2 -ODHP reaction on the 0.01Pt-5GaN/STO catalyst follows a mechanism of two-step coupling reaction between DDHP and RWGS reactions.

2. Experiment section

2.1. Chemicals and materials

All chemical reagents were used without any purification process. $SrTiO_3$ (99.5%), $BaTiO_3$ (99.5%), and $BiTiO_3$ (99.5%) materials were supplied by Aladdin Industrial Corporation. $Ga(NO_3)_3 \cdot xH_2O$ (>99.9%), methanol, $H_2PtCl_6 \cdot xH_2O$ (>99.9%), and urea were purchased from Macklin Inc., China. Additionally, all experimental gases used in the experiments were obtained from Xi'an Teda Cryogenic Equipment Co., Ltd.

2.2. Synthesis of Pt-GaN/ $SrTiO_3$ catalysts

The catalysts composed of STO supported GaN and Pt were prepared using a wet impregnation and *in situ* nitridation method, similar our previous works[17–20]. Initially, 0.50 g of STO was impregnated with a 1.50 mL methanol solution containing 0.07 g of $Ga(NO_3)_3 \cdot xH_2O$, a suitable amount of $H_2PtCl_6 \cdot xH_2O$ (prepared solution), and 0.12 g of urea. The impregnation was performed with sonication for 30 min,

followed by a 12-hour impregnation period. The impregnated sample was then dried at 60 °C for 8 h. Subsequently, the sample was transferred to a tube furnace under a nitrogen atmosphere and heated at 800 °C for 60 min at a heating rate of 1 °C/min. This process facilitated the *in situ* nitridation. After nitridation, the as-synthesized catalysts were collected and further subjected to decarburation at 550 °C for 4 h. Finally, the resulting catalysts were designated as 0.01Pt-5GaN/STO. For comparison purposes, other counterpart catalysts such as 0.01Pt/STO, 5GaN-/STO, 0.01Pt-5GaN/ $BaTiO_3$, 0.01Pt-5GaN/ $BiTiO_3$, and 0.01Pt-xGaN/STO were also prepared using the same procedure, and the 0.01 and 5 mean the Pt and Ga loadings, respectively.

2.3. Catalyst characterization

The X-ray diffraction (XRD) patterns were obtained using a Bruker D8 X-ray instrument fitted with Cu K α radiation (40 kv, 40 mA). The morphology of the catalyst was examined using a Scanning Electron Microscope (SEM) on an FEI Quanta 200 instrument. The valence information of the catalyst was provided by an ESCAL ab 220I-XL instrument. The CO_2 and C_3H_8 temperature-programmed desorption (CO_2 -TPD and C_3H_8 -TPD) profiles were recorded using a Micromeritics Autochem II 2920 chemisorption analyser equipped with a thermal conductivity detector. Electron paramagnetic resonance (EPR) tests were conducted on a Bruker A300 instrument to determine the oxygen vacancy (O_v) of the catalyst. The UV-Vis diffuse reflectance spectrum (UV-vis DRS) was acquired using a Cary 5000 spectrometer from Agilent, USA. *In situ* diffuse reflectance Fourier transform infrared spectroscopy (*in situ* DRIFTS) experiments were performed using a Bruker Tensor II spectrometer with a liquid nitrogen-cooling MCT detector.

2.4. Electrochemical measurements

The electrochemical impedance spectroscopy (EIS), linear sweep voltammetry curve (LSV), Mott Schottky, and amperometric current-time curves were conducted using a CHI660 electrochemical workstation (CH Instruments, Shanghai Chenhua Instruments Inc., China). For the reference electrode, a reversible hydrogen electrode (RHE) was utilized based on the conversion formula:

$$E_{RHE} = E(Ag/AgCl) + 0.197V + 0.059 \times pH$$

2.5. Computational details

We performed all density functional theory (DFT) calculations in a generalized gradient approximation (GGA) by the Perdew-Burke-Ernzerhof (PBE)[33] functional using the Vienna Ab initio Simulation Package (VASP)[34]. We chose the projected augmented wave (PAW) potential[35] to describe the ion nucleus and used a plane wave basis to consider the valence electrons with a kinetic energy cutoff of 400 eV. The van der Waals interactions were described by using the DFT-D3 empirical correction method. Geometry optimization with force convergence less than 0.05 eV/Å. All calculations use a $1 \times 1 \times 1$ gamma scheme k-points. The bottom atoms are fixed in all calculations. The Gibbs free energy (ΔG) of each electrochemical process was calculated as follows:

$$\Delta G = \Delta E + \Delta E_{ZPE} - T\Delta S$$

Among them, the values of ΔE , ΔE_{ZPE} , and ΔS are the changes of DFT energy, zero-point energy, and entropy at 573.15 k, respectively.

2.6. Catalytic performance test of photothermal CO_2 -ODHP

The catalytic performance of CO_2 -ODHP was evaluated in a photothermal reactor with a 180 mL capacity with a quartz lining. The reactor

had a quartz lining and a top sapphire window. The following steps were typically followed based on our previous work [21]. Twenty milligrams of the catalyst was evenly dispersed in the quartz lining. Then, the reactor was sealed and the air inside was removed under vacuum. A mixture gas of 30 mL of propane and 150 mL of CO₂ was injected into the reactor, and a top xenon lamp (300 W, CEL-HXF300, Beijing China Education Au-light Co., Ltd) was turned on. The lamp was located approximately 15 cm away from the catalyst, and the wavelength range was set between 300–1100 nm. Once the current from the xenon lamp stabilized, the electric furnace was turned on to reach the desired temperature. After the reaction, the outlet products were identified and analysed by using gas chromatography equipped with FID (flame ionization detector) and TCD (thermal conductivity detector). Hydrocarbons and olefins were analysed using an HP-AL/KCL capillary column (0.53 mm i.d., 15.0 μm film, 50 m length, Agilent Technologies Corp., Ltd.). CO₂ and CO were detected using a Porapak Q packed column and a GDX-502 column, respectively, along with a 5 Å molecular sieve column. The quantitative calculation formula related to catalytic performance are as follows:

$$C_i \text{ formation activity (mol·g}^{-1} \cdot h^{-1}) = \frac{\text{Produced molar of } C_i}{g \cdot h}$$

$$C_i \text{ Selectivity (\%)} = \frac{N_i \Phi_i}{\sum N_i \Phi_i}$$

In the given equations, C_i represents the target product, where i could be CH₄, C₂, C₃H₆, C₄, or CO. The Φ_i, g, and h stand for the volume fraction of the target product i, catalyst mass, and reaction time, respectively. N_i represents the number of carbon atoms in the product i.

3. Results and discussion

3.1. Catalytic performance

In catalytic performances studies, in view of GaN is a common semiconductor widely applied in photocatalysis, we initially investigated our previous developed catalysts in thermal catalytic CO₂-ODHP such as GaN/Na-ZSM-5(470) [18], GaN/KIT-6 [19], and GaN/Silicalite-1 [20], etc. However, all of them exhibited low activity, showing that the active site in these catalysts like Si-O-GaN-H could not work under the present photothermal conditions (Table 1, entries 1–3). The reaction could not occur in the absence of a catalyst, showing that it could not proceed spontaneously (entry 4). The sole GaN could catalyze the reaction but with a low C₃H₆ activity, confirming that the low intrinsic activity in the titled reaction (entry 5). Upon supported on STO, the GaN/STO showed an acceptable activity for propylene formation, but the CO yield is almost the same to that of STO (entries 7 vs 6). Compared with the performances obtained over the GaN/STO, the GaN, and the

STO, the interaction between GaN and STO contributes to the dehydrogenation of propane. Therefore, we speculated that the presence of GaN increased the adsorption activation site of C₃H₈, and the C₃H₈-TPD test results showed that the adsorption peak height of C₃H₈ adding GaN increased (Fig. S1), which confirmed the above speculation.

Interestingly, upon introduction of small amount of Pt (0.01 wt% tested by ICP-OES, Table S3), i.e., the Pt-GaN/STO catalyst, showed a great enhanced performance in producing C₃H₆ with 396.7 umol g_{cat}⁻¹ h⁻¹ and CO with 503.0 umol g_{cat}⁻¹ h⁻¹, 1.6-fold and 6.9-fold higher than those produced over the GaN/STO (entries 9 vs 7). These values are much higher than those reported photothermal catalysts in Table S1. Generally, the thermal catalysts could provide much higher activity in the reaction; however, they are always conducted at a higher reaction temperature (>500 °C) (Table S2). The results confirmed that the presence of Pt could promote the CO formation remarkably. Compared with the GaN/STO catalyst, the Pt/STO catalyst showed a higher CO activity, which also reflected the main role of Pt in the catalysis of CO₂ (entries 8 vs 7). The *in-situ* DRIFTS spectra confirmed that the Pt site probably acts as the active sites for CO₂ reduction, which will be discussed below. To further confirm the roles of GaN and Pt, we conducted some control experiments by using the 5GaN/STO and the 0.01Pt/STO catalysts in catalyzing both the direct dehydrogenation of propane (DHP) and reverse water-gas shift reaction (RWGS) reactions, with the results collected in Table S4. The DHP reaction was conducted in C₃H₈/N₂ atmosphere, while the RWGS reaction was proceeded in CO₂/H₂/N₂ atmosphere. Interestingly, the 5GaN/STO could achieve the DHP in the absence of CO₂, and the 0.01Pt/STO could catalyze the RWGS with a high activity, indicating that the GaN and Pt species could activate C–H bond in propane and C=O in CO₂, respectively. Interestingly, the Pt could enhance the photothermal effect via the localized surface plasmon resonance (LSPR), and the 0.01Pt-5GaN/STO shows that the highest temperature increases with irradiation time, which was supported by an IR thermal camera tested (Fig. S2).

The loading amount of GaN on the STO-based catalysts was examined, and the optimal loading was determined to be 5% (Table S5). In contrast to the 0.01Pt-5GaN/STO catalyst, the high loadings, i.e., 10 wt %, showed a slightly higher activity to C₃H₈, but a much lower yield of CO, supporting that the GaN species was probably the active site for C₃H₈. In addition, different photocatalytic active oxides were investigated, and their activities were lower than that of STO-based catalysts, indicative of the special nature of the STO material. The results demonstrated the interaction between GaN and STO is highly important for the reaction.

To examine the effect of light irradiation, we conducted the CO₂-ODHP reactions without light irradiation over the catalysts in Table 1, and the results are collected in Table S6. Compared with activities obtained under photothermal conditions, most of the catalysts offered

Table 1
Photothermal catalytic CO₂-ODHP over different typical catalysts.^[a]

Entry	Catalyst	C ₃ H ₈ Conv. (%)	Activity (μmol·g _{cat} ⁻¹ ·h ⁻¹)					C ₃ H ₆ Sele. ^[d] (%)
			C ₃ H ₆	CH ₄	C ₂ ^[b]	C ₄ ^[c]	CO	
1	5GaN/Na-ZSM-5	0.3±0	141.3±11	11.9±1	53.8±5	7.1±1	55.0±5	70.1±0.5
2	5GaN/KIT-6	0.2±0	127.2±13	9.4±1	53.1±4	7.6±1	46.9±4	71.4±0.8
3	5GaN/Silicalite-1	0.3±0	142.8±11	10.2±2	56.9±6	7.3±1	55.5±6	69.3±0.3
4	None	< 0.1	5.3±0.6	0.4±0.1	0.4±0.1	2.4±0.2	0.2±0	59.3±0
5	GaN	0.2±0	103.2±8	2.8±1	14.5±3	1.7±0.2	40.2±3	83.1±0.2
6	STO	0.3±0	112.7±9	1.4±0.2	18.9±2	6.1±0.9	60.4±4	83.2±0.8
7	5GaN/STO	0.6±0.1	247.3±19	3.5±0.5	29.5±6	7.0±1	69.7±8	88.2±1
8	0.01Pt/STO	0.3±0	168.1±12	4.6±1	30.7±5	8.7±1	141.6±13	82.4±1
9	0.01Pt-5GaN/STO	1.1±0.2	396.7±26	12.9±2	57.2±6	12.8±1	503.0±39	87.3±2
10	0.01Pt-5GaN/BaTiO ₃	0.2±0	102.2±7	2.0±0.6	23.7±3	4.1±0.6	78.4±4	82.1±0.4
11	0.01Pt-5GaN/BiTiO ₃	0.3±0	139.3±8	5.2±1	27.0±3	8.3±2	63.4±3	81.2±0.1
12	0.01Pt-5GaN/TiO _x	0.4±0	176.3±14	6.2±2	26.2±4	7.5±1	94.6±7	85.6±0.4

[a] Reaction conditions: catalyst 20 mg, C₃H₈/CO₂ 1/5, total volume 180 mL, 300 °C, 1 h, and 300 W Xe lamp full irradiation. [b] C₂ includes ethane and ethylene. [c] C₄ includes n-butane, isobutane, n-butene, and isobutene. [d] Selectivity of propylene in total olefins.

lower activities of propylene, indicating that the light illumination indeed promotes the reaction. Importantly, the 0.01Pt-5GaN/STO catalyst delivered the highest activity under photothermal conditions, which is much higher than that under thermal conditions (Table 1 entry 9 vs Table S6 entry 9).

The contrast experiments under photo and thermal conditions, as well as the substitution of N₂ for CO₂ showed that the thermal condition and the presence of CO₂ are the main factors for improving the catalytic performances of the reaction (Fig. 1a). The optimized reaction conditions indicated that increasing the reaction temperature and prolonging the reaction time can improve the yields of propylene and CO (Fig. 1b and c). The high temperature indeed promotes the reaction, not only for the heating conditions could reduce the band gap width[36], but also reduce the reduction potential of CO₂[37] and improve the oxidation potential of propane, and thus enhancing the catalytic performances of photothermal CO₂-ODHP. The reusability of the catalyst was assessed through alternating photothermal and thermal cycles (Fig. 1d). After 17 cycles, the formation activity of propylene decreased to below 300 μmol·g_{cat}⁻¹·h⁻¹. The results not only proved the high stability of the catalyst (Fig. 1d and Fig. S3) but also confirmed the light significantly enhances the reaction remarkably. In addition, under flowing reaction gases, the yield of propylene was initially 275.2 μmol·g_{cat}⁻¹·h⁻¹ at 1 h, which was maintained at 248.7 μmol·g_{cat}⁻¹·h⁻¹ after continuous testing at 6 h and a flow rate of 6 mL/min (C₃H₈/CO₂ = 1/5) (Fig. S4). These findings affirm that the catalyst has good stability. The used samples were characterized by XRD, demonstrating a similar phase to the fresh one and its stability (Fig. S5).

Indeed, the CO₂ oxidative dehydrogenation of propane (CO₂-ODHP) is a complex reaction, which involves C₃H₈, C₃H₆, CO₂, CO, H₂O, H₂, etc. Together with these products, some fragment components such as CH₄, CH₃CH₃, CH₂CH₂, etc. stemmed from the inevitable cracking are always detected. The produced C₃H₆ could be potentially coupled with these fragments, especially with CH_x species to C₄ species on the surface of

catalyst.

3.2. Catalyst characterization photoelectric properties tests

The catalyst was characterized by using diverse technologies. Initially, the sample showed an aggregated particles morphology, which was confirmed by SEM image (Fig. S6). The HRTEM confirmed the lattice spacings of 0.260 nm assigned to (100) planes of GaN, of 0.225 nm indexed to (111) planes of Pt, and of 0.276 or 0.275 nm corresponding to the (110) planes of STO, respectively (Fig. 2c and d). It is worth noting that together with the GaN and Pt particles, the highly dispersed GaN and Pt were also present, and this was supported by the EDS images (Fig. 2a and b). The Pt species exist both in aggregated nanoparticles and monodispersed component, although its loading is only 0.01%. The Pt NPs were also confirmed by the following *in situ* DRIFTS results, which showed a CO at 2075 cm⁻¹, assigning to the Pt NPs coordination sites with CO, and this will be further discussed below. The bulk phase composition of the samples was also examined (Fig. 2e), and the main bulk phase could be assigned to STO (JCPDS NO. 35-0734). This confirms the main structure of STO was not destroyed during the preparation procedures[38]. No obvious peaks of GaN and Pt NPs were found for the low loading and high dispersion. To support the formation of GaN, we tested the XRD patterns of the catalysts with Ga loading of 10% and 15%, with the results given in Fig. S7. In the XRD pattern of the 0.01Pt-15GaN/STO, some characteristic diffraction peaks appeared at 32.4, 34.7, 36.9, 48.2, 69.2, and 72.9° attributed to (100), (002), (101), (102), (112), and (004) crystal faces of GaN, respectively, supporting that GaN was formed during the preparation of catalyst. Besides, to further confirm the generation of GaN from Ga(NO₃)₃·xH₂O with urea, we calcinated the Ga(NO₃)₃·xH₂O with urea at 800 °C and followed by a decarbonization step, and the obtained solid was corroborated to GaN by the XRD patterns in Fig. S7b. However, the Ga(NO₃)₃·xH₂O calcinated at 800 °C under N₂ could not be transferred into GaN, verified by

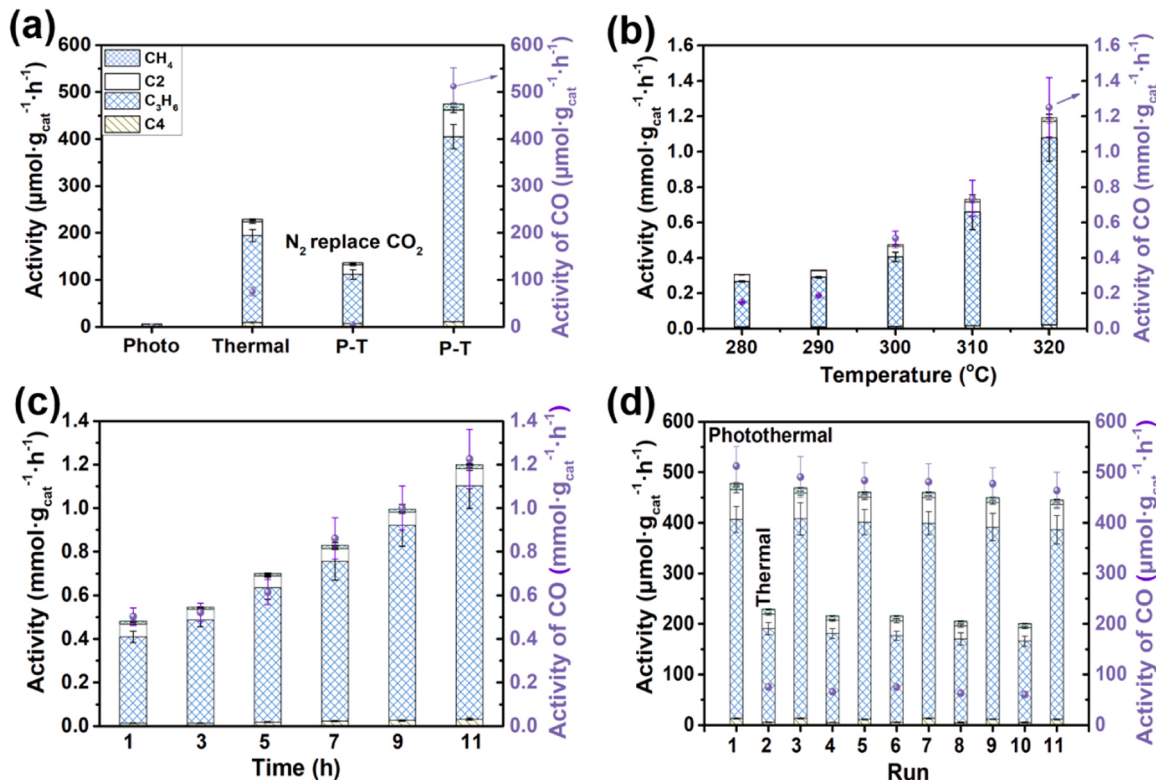


Fig. 1. Catalytic performances of CO₂-ODHP over the 0.01Pt-5GaN/STO (a) under different reaction conditions, (b) at different reaction temperatures, and (c) for different reaction time. (d) The reusability of the 0.01Pt-5GaN/STO catalyst. P-T is photo-thermal. Reaction conditions: catalyst 20 mg, C₃H₈/CO₂ 1/5, total volume 180 mL, 300 °C (a, c, d), 1 h (a, b, d), and 300 W Xe lamp full irradiation.

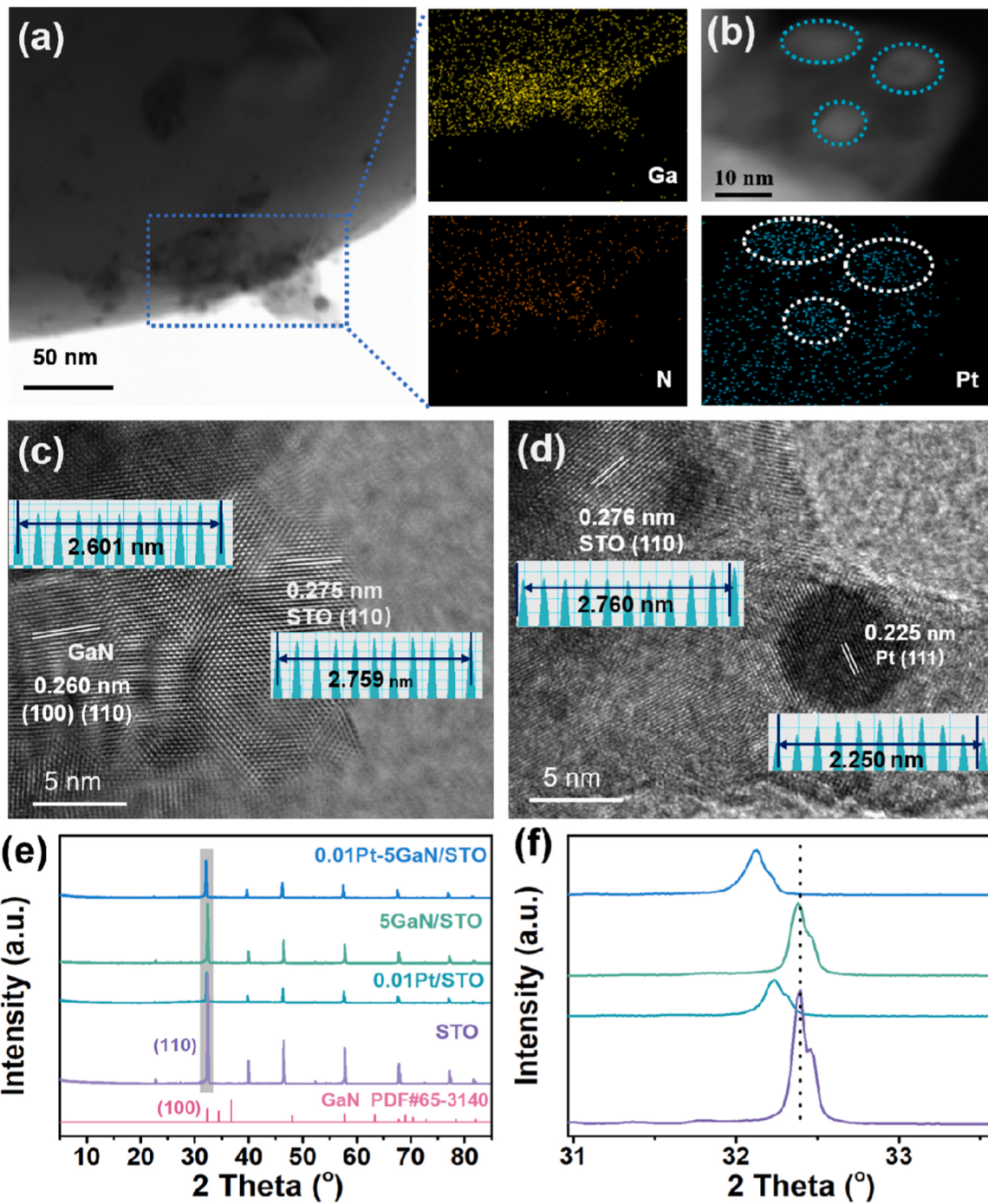


Fig. 2. Structural characterization of the Pt-GaN/STO composites, (a and b) TEM and EDS patterns, (c and d) HRTEM images, (e) XRD patterns of diverse catalysts, and (f) enlarged image of XRD.

the XRD in Fig. S7b, showing that the no additional nitrogen sources could not generate GaN. Interestingly, in Fig. 2f, the peaks at approximately 32° assigned to the (110) planes of STO were slightly shifted, indicated that the Pt species was incorporated into STO perovskite lattice[39].

The full XPS spectra of the catalysts are depicted in Fig. S8. The survey XPS spectra indicate the characteristic signal peaks corresponding to O 1 s, Ti 2p, and Sr 3d regions, respectively (Fig. 3). In the Sr 3d XPS spectra, two sets of the fitted peaks at 132.5, 134.4 eV and 133.6, 135.4 eV were assigned to the 3d_{5/2} and 3d_{3/2} XPS peaks of Sr²⁺ in perovskite and Sr-based suboxide (Fig. 3a)[40]. Upon loading GaN, the proportion of Sr assigned to suboxide species increased remarkably,

confirming a decrease in the content of perovskite oxide species. This change probably correlates with alterations in surface oxygen species. Specifically, upon loading GaN, it could react with lattice oxygen in STO, and form Ga-O species. Consequently, O_v were generated. The XPS spectra of Ti 2p observed at 457.6, 463.2 eV, and 458.1, 463.9 eV can be attributed to the characteristic signals of Ti³⁺ and Ti⁴⁺ (Fig. 3b)[41]. Table S7 presents the valence state of Ti remains constant from the STO to the 0.01Pt-5GaN/STO. The XPS spectra of O 1 s were fitted into two peaks assigned to adsorbed oxygen (O_{ads}) at 531.3 eV and lattice oxygen (O_{lat}) at 528.9 eV[42] (Fig. 3c). Detailed information indicates that the content of O_{lat} gradually diminishes while O_{ads} increases with the loading of GaN and Pt (Table S7). In addition, Fig. S9 provides XPS

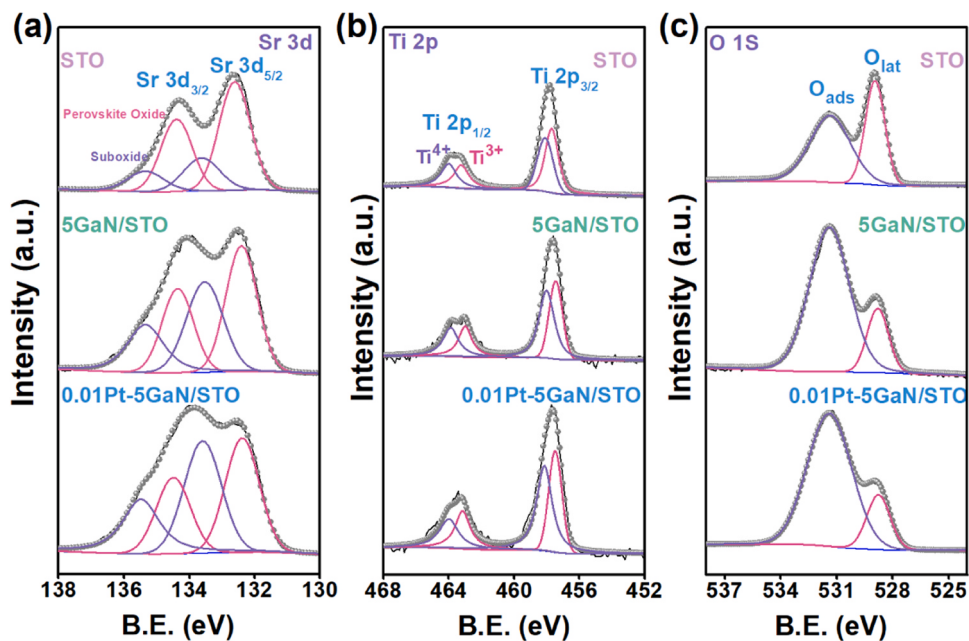


Fig. 3. (a) Sr 3d, (b) Ti 2p, and (c) O 1 s XPS spectra of the STO, 5GaN/STO, and the 0.01Pt-5GaN/STO, respectively.

spectra of Pt and Ga, indicative of their valances of Pt⁰, Pt²⁺, and Ga³⁺.

Based on the XPS results, the increase of O_{ads} may lead to enhanced adsorption and activation of CO₂ molecule through the O_v. The EPR test results indicate the presence of distinct characteristic peaks corresponding to O_v after loading GaN onto STO (Fig. S10). Compared to the EPR curve of the STO, after loading of GaN, the peak at g-value of 2.01

linked to the O_v increased remarkably, showing the GaN could introduce the O_v formation on the sample. However, upon incorporation of Pt, the same peak exhibits a semblable curve as the GaN/STO, confirming that the Pt contributes less to O_v. The greatly enhancement after introduction of Pt, especially in CO formation, was probably due to the cooperation of Pt with O_v, which promotes the adsorption and activation of CO₂.

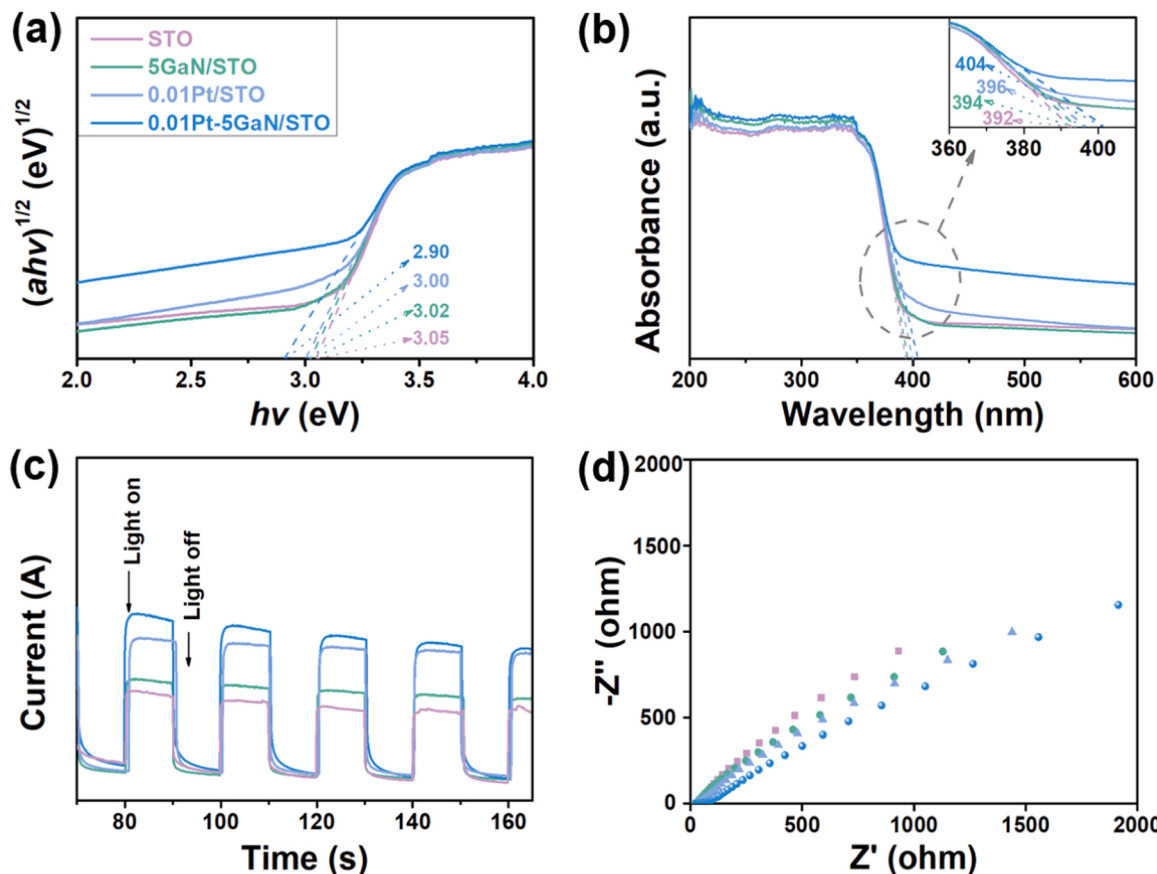


Fig. 4. (a) UV-vis DRS spectra, (b) Kubelka-Munkplots, (c) transient photocurrent response, and (d) EIS Nyquist plots of diverse catalysts.

Distinguished to the previous reported BiOI-based catalysts[21,22], the present Pt-GaN/STO catalyst could not catalyse the CO₂ reduction by only using O_v.

Importantly, it is worth noting that the O_v increased upon GaN loading. This is because there is a strong interaction between GaN and the STO carrier via the formation of Ga-O species, which further reduces the lattice oxygen content but increases the oxygen vacancy content. [18–20] On the other hand, the existence of O_v can induce the formation of defect levels lower than the conduction band (CB) level in STO when subjected to visible light irradiation, thus generating electron-hole pairs [43]. Interestingly, the EPR detection exhibited a strong Ti³⁺ signal. It has been reported that the coexistence of Ti³⁺ and O_v can induce the formation of an in-gap band, thereby enhancing the absorption of visible light[44].

The adsorption edge of STO was observed at 392 nm, which is examined by the UV-vis DRS (Fig. 4a), and the results are consistent

with literature reports[45]. After loading GaN, Pt, and Pt-GaN, the absorption edge gradually shifted towards the visible range. Compared with the other samples, the band gap of the 0.01Pt-5GaN/STO catalyst was lower, based on the Tauc plots converted using the Kubelka-Munk method (Fig. 4b), indicating that the light irradiation promotes the electron-hole separation. The shift of the adsorption edge towards the visible range and the small band gap of the 0.01Pt-5GaN/STO catalyst indicate an enhanced potential for the generation of free electrons under light irradiation. The transient photocurrent response and electrochemical impedance spectroscopy (EIS) Nyquist plots were measured using the electrochemical method. The 0.01Pt-5GaN/STO catalyst exhibits the highest current response under light irradiation compared to others, indicating that the catalyst possesses the highest photo response (Fig. 4c). The 0.01Pt-5GaN/STO catalyst exhibits a smaller arc radius in the Nyquist plot (Fig. 4d), confirmed that it has the lowest electrical resistance, and this is beneficial for the electron-hole generation,

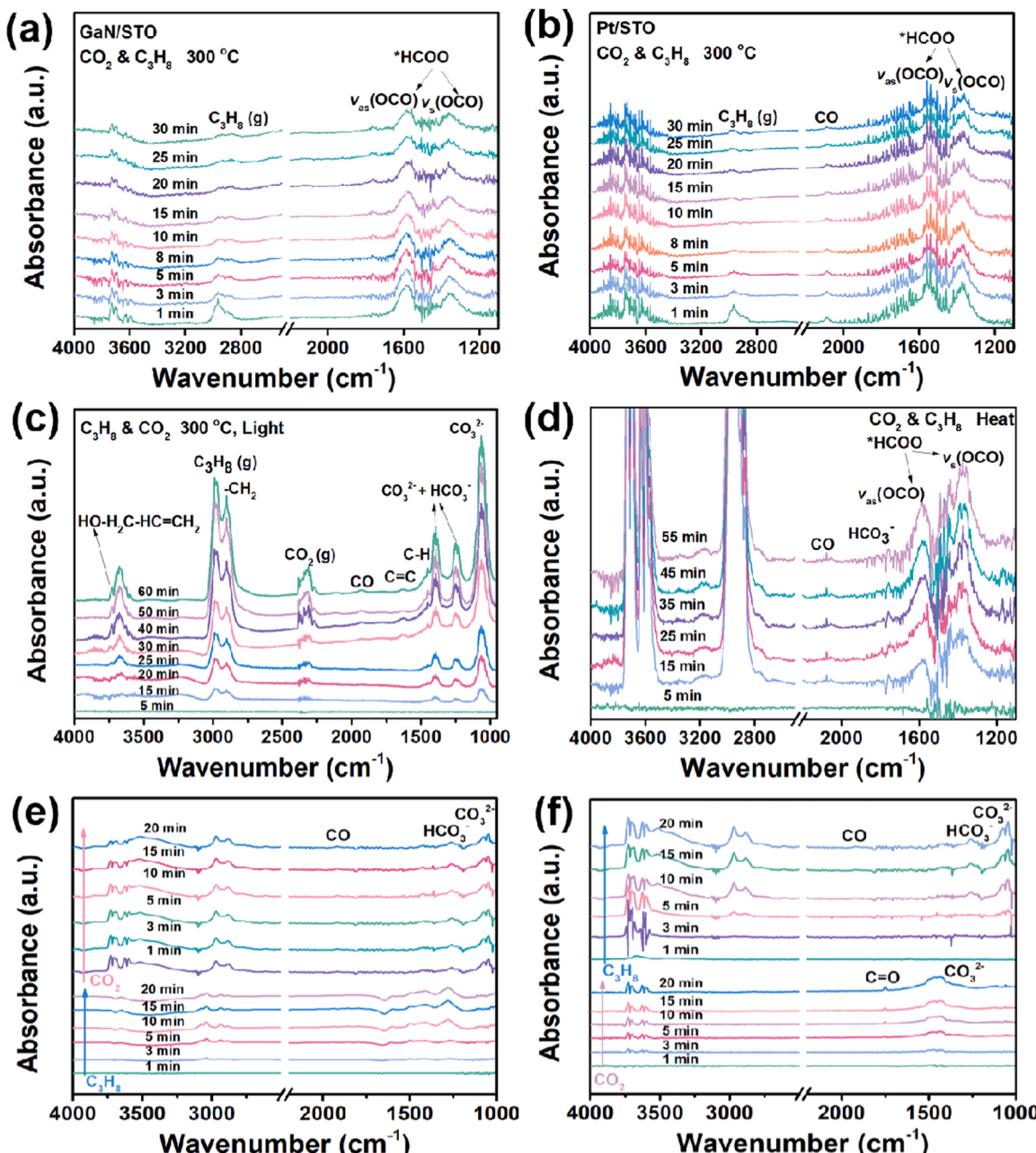


Fig. 5. *In situ* DRIFTS spectra of the (a) 5GaN/STO, (b) 0.01Pt/STO, and (c-f) 0.01Pt-5GaN/STO catalysts, respectively. Reaction conditions: (a), (b), and (d) at 300 °C without light illumination; (c, e, and f) at 300 °C with light illumination.

separation, transfer, and improved photocatalytic performance. These photoelectronic properties tests indicated that the incorporation of Pt could improve the light utilization rate and the electron transfer rate, which was probably due to the rapid transfer of photogenerated electrons from GaN and STO to the Pt nanoparticles, thus reducing the recombination of photogenerated charge carriers.

The VB and flat-band potential of the STO-based catalysts were measured (Fig. S11). The flat-band potential values of STO, obtained from Mott-Schottky curves, were consistent with literature reports[46]. Upon loading GaN and Pt onto STO, the flat-band potential shifted towards higher potential energy. This shift can be attributed to the increased concentration of O_v, which in turn causes the Fermi level to shift towards higher energies[47]. These observations align with the results obtained from XPS and EPR tests. Moreover, the band structure of the catalysts was determined based on the CB, band gap, and flat-band potential (Fig. S12).

3.3. In-situ DRIFTS tests

To evaluate the performance of individual components in the 0.01Pt-5GaN/STO catalyst, *in-situ* DRIFTS characterization was employed to investigate the intermediates involved in the CO₂-ODHP reactions of the 0.01Pt/STO and 5GaN/STO catalysts separately (Fig. 5a and b). Both graphs showed similar adsorption peaks of CO₂ intermediate states at 1600–1200 cm⁻¹. However, a distinct signal observed in the 0.01Pt/STO catalyst was the presence of a CO linear stretching vibration, supported by the peak at 2075 cm⁻¹, which was not observed in the 5GaN/STO catalyst. This finding provides evidence that Pt primarily serves as the active catalyst for CO₂ conversion in the reaction even its low loading (0.01%). The presence of Pt contributes to the formation of the CO intermediate, which is crucial for the subsequent production of propylene, and this will be discussed in the following DFT calculations.

In Fig. 5c, under light irradiation, the peaks observed in the range of 3600–3100 cm⁻¹ are attributed to the stretching vibration of the hydroxyl group of adsorbed water on the catalyst surface, with a prominent peak at 3735 cm⁻¹ corresponding to the hydroxyl group of allyl alcohol [48]. The peaks observed in the range of 3050–2800 cm⁻¹ are associated with the C-H vibrations of CH₃ and CH₂ species of adsorbing gaseous propane[49]. The peak observed in the range of 2400–2250 cm⁻¹ corresponds to gaseous CO₂[50]. It is noteworthy that the C=C and C-H stretching vibration peaks of propylene were detected at 1630 and 1460 cm⁻¹[51,52], indicating the presence of propylene. The peaks in the 1075–1044 cm⁻¹ range are associated with CO₃²⁻ [53,54], while the peaks at the range of 1248–1220 cm⁻¹[55,56] and 1405–1380 cm⁻¹[57, 58] can be attributed to carbonate and bicarbonate species (Fig. 5c). The peaks observed in the 1589–1562 cm⁻¹ and 1380–1359 cm⁻¹ range can be attributed to the asymmetric and symmetrical OCO stretching vibrations of the bidentate *HCOO species[59,60], respectively (Fig. 5d). Additionally, some weak peaks at 1750 cm⁻¹ were corresponding to HCO₃[58]. These findings suggest that the *HCOO species plays a critical role as an intermediate in CO formation in the thermal CO₂-ODHP; however, the carbonate and bicarbonate species are involved in the photothermal CO₂-ODHP.

To further investigate the possible intermediates of the reaction, we separately introduced CO₂ and C₃H₈ gases across the catalyst and conducted the *in situ* DRIFTS tests, with the results collected in Fig. 5e and f. Upon introduction C₃H₈, various peaks appeared between 1600 and 1000 cm⁻¹ assigned to the C-C vibrations of free propane molecule[60], and new signals were generated after the introduction of CO₂, which were respectively attributed to carbonate, bicarbonate, and CO (Fig. 5e). The similar phenomenon could be found by initially introducing CO₂ and followed by C₃H₈. Upon introduction CO₂, CO₃²⁻ species could be also found. Followed that by introducing C₃H₈, two new wide peaks appeared at 3100–2800 cm⁻¹, which could be ascribed to C-H stretching vibration peaks (Fig. 5f). Besides, the peaks at 1800–1000 cm⁻¹ assigned to HCO₃ and CO₃²⁻ species[60,61] could also be found, indicating that the

present catalyst under photothermal conditions really involved carbonate and bicarbonate intermediates in CO₂-ODHP.

Interestingly, the characteristic frequencies of CO under thermal and photothermal conditions appeared at 2075 cm⁻¹ and 1930 cm⁻¹, respectively, indicating the presence of two adsorption forms of CO, i.e., linear adsorption and bridge configuration on Pt nanoparticles, respectively[62]. This may be due to the difference in reaction temperature and/or CO coverage (Fig. 5 and Fig. S13). No CO signal was detected on monodispersed Pt species, which characteristic peak > 2100 cm⁻¹[62], indicating that the Pt NPs is probably the active site in activating CO₂ in the present catalyst. As mentioned above, the CO₂-TPD experiments show that STO-based catalyst has good adsorption performance for CO₂ (Fig. S1). For photothermal catalysis, CO₂ was converted into CO via the intermediates of carbonate and bicarbonate species, while for thermal catalysis, with a low activity, CO₂ was transferred via *HCOO. The *in-situ* DRIFTS results confirmed that two pathways are involved in the photothermal and thermal CO₂-ODHP reactions, respectively. In this respect, different intermediates are involved in CO₂ conversion for the RWGS reaction in the thermal CO₂-ODHP and the photothermal CO₂-ODHP routes. These findings elucidate the mechanistic differences between the two reaction conditions and provide valuable insights into the pathways and intermediates involved in the conversion of CO₂ to CO.

3.4. DFT calculation and catalytic mechanism

To validate the mechanism of the Pt-GaN/STO catalyzed photothermal CO₂-ODHP, the key intermediates and potential energy profiles were studied by DFT calculation. According to former structure characterizations, we modeled and optimized the structure of the Pt-GaN/STO catalyst with O_v (Fig. S14). Two reaction pathways of CO₂-ODHP were studied by calculating the intermediate state and standard Gibbs free energy (ΔG) at 300 °C (Fig. 6a and b). On the GaN surface, C₃H₈ is activated to C₃H₈^{*} (0.68 eV), and then dehydrogenated to C₃H₆ and 2 H^{*} (-0.95 eV) (Fig. S15). Meanwhile, CO₂ is activated on Pt NPs to CO₃²⁻ (-0.64 eV), then forming CO₃^{*} (-1.47 eV) with surface O_{lat} (Table S8). It is then combined with H^{*} to form *HCOO (0.75 eV) and HCO₃^{*} (0.32 eV), respectively, and then hydrogenated to CO and H₂O (Figs. S16 and S17). Among them, the ΔG required for the desorption of *HCOO and HCO₃^{*} into CO and H₂O after reacting with H^{*} are 1.24 and 1.29 eV (Table S8), respectively, which are the rate-determining step of the reaction. The rate-determining steps showed a small difference. The difference between the two paths is due to the formation of different intermediate states. Obviously, in photothermal catalysis, CO₂ could be converted into CO via the CO₃^{*} intermediate, which possesses the lowest active energy, indicating the CO₃^{*} is easily formed during the reaction. However, the subsequent steps require overcoming higher energy barriers, thus, in this viewpoint, the photothermal route seems to be unadvantageous. It is worth noting that the present calculation on photothermal routes did not take into account the contribution from light irradiation. Together with the experiments, the calculation results confirmed that the important role of the light, which could provide more energy to cross the activation energy barrier.

The reaction transition state and reaction energy barrier were further calculated by the kinetic investigation of the rate-determining step (Fig. 6c and d). One route (purple color) involves that *HCOOH+H^{*} (IS-a1) goes through HCOOH^{*} (TS-a1), HCO^{*}+OH^{*} (IS-a2), and CO^{*}+H₂O^{*} (TS-a2) to CO₂+H₂O (FS-a), while another route is that (pink color) *HCO₃⁺+H^{*} (IS-b1) pass through HCO₃²⁻+H^{*} (TS-b1), HCO₂^{*}+OH^{*} (IS-b2), and CO^{*}+H₂O^{*} (TS-b2) to CO+H₂O (FS-b). The first route requires the activation energy of 2.72 eV, and the second needs 2.11 eV. This result shows that the reaction energy barrier of the photothermal (carbonate intermediate) reaction is smaller than that of the thermal (formate intermediate) reaction, so it is proved that the photothermal reaction is easier to carry out from the perspective of dynamics.

In addition, the Bader charge calculates the electronic behaviour of

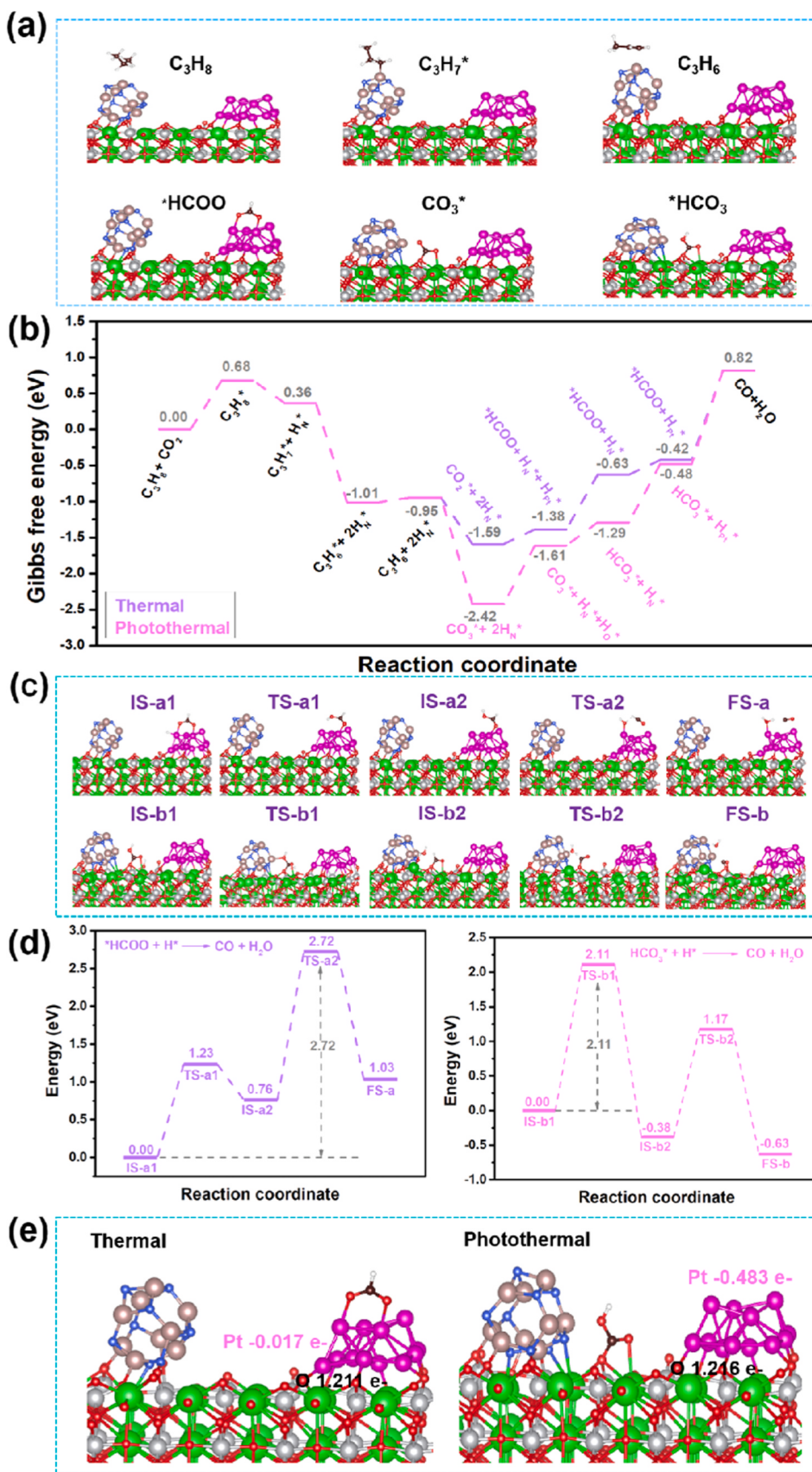


Fig. 6. C_3H_8 and CO_2 activations on Pt-GaN/STO (a), the Gibbs free energy diagrams of CO_2 -ODHP on the Pt-GaN/STO (b), corresponding intermediates and transition states (TS) (c), TS energy barrier diagram (d), and Bader charge diagram on different intermediates (e).

the two intermediate states. In the photothermal (carbonate intermediate) route, in the structural configuration of catalyst adsorbed $^*\text{HCO}_3$, the gain electrons of the Pt species are 0.483 e⁻, and the loss electrons of the O near O_v are 1.216 e⁻, while in the thermal (formate intermediate) route, in the structural configuration of catalyst adsorbed $^*\text{HCOO}$ intermediate, the gain electrons of Pt species are 0.017 e⁻ and the loss electrons of the O close to O_v are 1.211 e⁻, respectively (Fig. 6e). These results revealed that the more electrons favor to transfer to Pt in the photothermal process, which is beneficial for the following reaction. Therefore, DFT calculations provided the energy of different reaction pathways of the CO₂-ODHP over the Pt-GaN/STO catalyst, and the results further confirm the crucial role of light in the reaction.

The light illumination is highly important for the present catalytic reaction, since it could enhance the local temperature on the active sites, which was confirmed by the infrared thermal imaging testing in Fig. S2. Besides, the light introduction could excite electrons in the catalyst, further promoting the reaction, and this was corroborated by the photoelectronic properties study in Fig. 4. Introducing light, the photothermal CO₂-ODHP over the Pt-GaN/STO catalyst could be conducted via a different way compared with the conventional thermal way. Thus, the light illumination could change the reaction pathway of the CO₂-ODHP, and this was supported by the *in-situ* DRIFTS testing and DFT calculation.

Indeed, the CO₂-ODHP is a complicated reaction, and other reactions such as the formation of deposited carbon, reverse Boudouard reaction, RWGS reaction, and DDHP are always involved during the reaction. Thus, it is very difficult to discover the catalytic mechanism of the CO₂-ODHP. Generally, to produce propylene, at least two mechanisms are widely accepted, *i.e.*, MvK mechanism and coupling of RWGS and DDHP. In the former MvK mechanism, the O_{lat} on the catalyst is always recognized as active sites, which could activate propane to propylene by forming water. As for the coupling reactions mechanism, propane is initially dehydrogenated to propylene and H₂, and CO₂ reacted with H₂ to shift the reaction equilibrium to produce more propylene.

It is worth mentioning that the working mechanism depends on the catalytic system applied and operated conditions. In photothermal catalytic processes, these two reaction mechanisms probably still work. Compared with the conventional thermal catalysis, the photothermal route, especially conducted at low temperatures, neither the DDHP nor the RWGS are feasible to occur since both are endothermic reactions. However, with the promotion of photo and excited electron-hole pairs, the reaction will produce unexpected results under milder conditions, especially at low temperatures.

Based on comparative experiments, *in situ* DRIFTS, and C₃H₈-TPD, GaN and Pt were confirmed as the main active centers of C₃H₈ and CO₂, respectively. Combined with the DFT calculation results, we propose a reasonable mechanism for the photothermal CO₂-ODHP and thermal CO₂-ODHP reactions. The process begins with the activation and dissociation of propane molecules on GaN, forming C₃H₇^{*} and H^{*}. Concurrently, CO₂ molecules are activated by Pt and adsorbed by O_v on STO. The CO₂ molecules bond with O_{lat} to create CO₃^{*}. Moreover, H^{*} reacts with CO₃^{*} to form HCO₃^{*}. Subsequently, C₃H₇^{*} continues to dissociate into C₃H₆ and H^{*}, while H^{*} combines with HCO₃^{*} to produce CO and H₂O, releasing O_{lat} in the process. Additionally, the thermal CO₂-ODHP reaction, propane molecules undergo activation and dissociation on GaN, resulting in the formation of C₃H₇^{*} and H^{*}. These species interact with activated CO₂ and H^{*} to form $^*\text{HCOO}$ intermediates. Following this, C₃H₇^{*} further dissociates into C₃H₆ and H^{*}, while H^{*} reacts with $^*\text{HCOO}$ to yield CO and H₂O.

4. Conclusion

In conclusion, we have successfully developed highly active dual-functional catalysts for the photothermal CO₂-ODHP. The characterization results revealed that the incorporation of GaN leading to the creation of O_v, the Pt particles improved the light utilization efficiency,

photothermal effect via LSPR, electron transport rate, and CO₂ activation capacity of the catalyst. Experimental data and *in situ* DRIFTS analysis provided GaN primarily activates the C-H bonds, while Pt predominantly activates the C=O bonds in the CO₂ molecule. Moreover, *in situ* DRIFTS testing uncovered distinct transition states for CO₂ transformation in the thermal and photothermal CO₂-ODHP reactions. The activation energies of these transition states were determined through DFT calculations. By integrating the catalytic data, *in situ* DRIFTS observations, and DFT calculations, we present compelling evidence that the coupling mechanism of photothermal CO₂-ODHP with the 0.01Pt-5GaN/STO catalyst follows the DDHP and RWGS pathway. Overall, these results contribute to the development of efficient and sustainable strategies for propylene supply and carbon neutrality.

CRediT authorship contribution statement

Sen-Wang Wang: Investigation, Writing – original draft, Formal analysis. **Zhen-Hong He:** Conceptualization, Methodology, Writing – original draft, Investigation. **Yue Tian:** Investigation, Writing – review & editing. **Zhan-Jun Zhu:** Formal analysis. **Yong-Chang Sun:** Partial activity tests. **Kuan Wang:** Supervision. **Weitao Wang:** Investigation. **Yang Yang:** Investigation. **Huan Wang:** Investigation. **Zhao-Tie Liu:** Supervision, Funding acquisition, Writing – review & editing.

Declaration of Competing Interest

The authors declare that they have no known competing financial interests or personal relationships that could have appeared to influence the work reported in this paper.

Data Availability

Data will be made available on request.

Acknowledgements

The authors gratefully acknowledge the financial supports from National Natural Science Foundation of China (22078182 and 22278261), the Key Project of Education Department of Shaanxi Province (21JY005).

Appendix A. Supporting information

Supplementary data associated with this article can be found in the online version at doi:10.1016/j.apcatb.2024.124246.

References

- [1] S. Chen, X. Chang, G. Sun, T. Zhang, Y. Xu, Y. Wang, C. Pei, J. Gong, Propane dehydrogenation: catalyst development, new chemistry, and emerging technologies, Chem. Soc. Rev. 50 (2021) 3315–3354, <https://doi.org/10.1039/D0CS00814A>.
- [2] Y. Dai, X. Gao, Q. Wang, X. Wan, C. Zhou, Y. Yang, Recent progress in heterogeneous metal and metal oxide catalysts for direct dehydrogenation of ethane and propane, Chem. Soc. Rev. 50 (2021) 5590–5630, <https://doi.org/10.1039/D0CS01260B>.
- [3] E. Gomez, Z. Xie, J.G. Chen, The effects of bimetallic interactions for CO₂-assisted oxidative dehydrogenation and dry reforming of propane, AIChE J. 65 (2019) e16670, <https://doi.org/10.1002/aic.16670>.
- [4] G. Li, C. Liu, X. Cui, Y. Yang, F. Shi, Oxidative dehydrogenation of light alkanes with carbon dioxide, Green. Chem. 23 (2021) 689–707, <https://doi.org/10.1039/D0GC03705B>.
- [5] J. Wang, Y.H. Song, Z.T. Liu, Z.W. Liu, Active and selective nature of supported CrOx for the oxidative dehydrogenation of propane with carbon dioxide, Appl. Catal. B-Environ. 297 (2021) 120400, <https://doi.org/10.1016/j.apcatb.2021.120400>.
- [6] M.L. Balogun, S. Adamu, I.A. Bakare, M.S. Ba-Shammakh, M.M. Hossain, CO₂ assisted oxidative dehydrogenation of propane to propylene over fluidizable MoO₃/La₂O₃- γ Al₂O₃ catalysts, J. CO₂ Util. 42 (2020) 101329, <https://doi.org/10.1016/j.jcou.2020.101329>.

- [7] J. Baek, H.J. Yun, D. Yun, Y. Choi, J. Yi, Preparation of highly dispersed chromium oxide catalysts supported on mesoporous silica for the oxidative dehydrogenation of propane using CO₂: insight into the nature of catalytically active chromium sites, *ACS Catal.* 2 (2012) 1893–1903, <https://doi.org/10.1021/cs300198u>.
- [8] S. Lawson, K.A. Newport, A. Axtell, C. Boucher, B. Grant, M. Haas, M. Lee, F. Rezaei, A.A. Rownaghi, Structured bifunctional catalysts for CO₂ activation and oxidative dehydrogenation of propane, *ACS Sustain. Chem. Eng.* 9 (2021) 5716–5727, <https://doi.org/10.1021/acssuschemeng.1c00882>.
- [9] M. Kantserova, N. Vlasenko, S. Orlyk, K. Veltruska, I. Matolinova, Effect of acid-base characteristics of In₂O₃-Al₂O₃(ZrO₂) compositions on their catalytic properties in the oxidative dehydrogenation of propane to propylene with CO₂, *Theor. Exp. Chem.* 55 (2019) 207–214, <https://doi.org/10.1007/s11237-019-09610-9>.
- [10] H. Wang, G. Tsilomelekis, Catalytic performance and stability of Fe-doped CeO₂ in propane oxidative dehydrogenation using carbon dioxide as an oxidant, *Catal. Sci. Technol.* 10 (2020) 4362–4372, <https://doi.org/10.1039/D0CY00586J>.
- [11] L. Annamalai Kim, R.F. Lobo, Silica-encapsulated Fe₂O₃ oxygen carriers for selective chemical looping combustion of hydrogen, *Chem. Eng. J.* 455 (2023) 140919, <https://doi.org/10.1016/j.cej.2022.140919>.
- [12] E. Gomez, S. Kattel, B. Yan, S. Yao, P. Liu, J.G. Chen, Combining CO₂ reduction with propane oxidative dehydrogenation over bimetallic catalysts, *Nat. Commun.* 9 (2018) 1398, <https://doi.org/10.1038/s41467-018-03793-w>.
- [13] E. Nowicka, C. Reece, S.M. Althabban, K.M. Mohammed, S.A. Kondrat, D. J. Morgan, Q. He, D.J. Wilcock, S. Golunski, C.K. Kiely, Elucidating the role of CO₂ in the soft oxidative dehydrogenation of propane over ceria-based catalysts, *ACS Catal.* 8 (2018) 3454–3468, <https://doi.org/10.1021/acscatal.7b03805>.
- [14] R. Jin, J. Easa, D.T. Tran, C.P. O'Brien, Ru-Promoted CO₂ activation for oxidative dehydrogenation of propane over chromium oxide catalyst, *Catal. Sci. Technol.* 10 (2020) 1769–1777, <https://doi.org/10.1039/C9CY01990A>.
- [15] B. Yan, S. Yao, S. Kattel, Q. Wu, Z. Xie, E. Gomez, P. Liu, D. Su, J.G. Chen, Active sites for tandem reactions of CO₂ reduction and ethane dehydrogenation, *Proc. Natl. Acad. Sci.* 115 (2018) 8278–8283, <https://doi.org/10.1073/pnas.1806950115>.
- [16] F. Xing, Y. Nakaya, S. Yasumura, K. i Shimizu, S. Furukawa, Ternary platinum–cobalt–indium nanoalloy on ceria as a highly efficient catalyst for the oxidative dehydrogenation of propane using CO₂, *Nat. Catal.* 5 (2022) 55–65, <https://doi.org/10.1038/s41929-021-00730-x>.
- [17] L. Zhang, Z.Y. Wang, J. Song, Y. Lang, J.G. Chen, Q.X. Luo, Z.H. He, K. Wang, Z. W. Liu, Z.T. Liu, Facile synthesis of SiO₂ supported GaN as an active catalyst for CO₂ enhanced dehydrogenation of propane, *J. CO₂ Util.* 38 (2020) 306–313, <https://doi.org/10.1016/j.jcou.2020.02.010>.
- [18] Z.Y. Wang, Z.H. He, Y. Xia, L. Zhang, K. Wang, W. Wang, Y. Yang, J.G. Chen, Z. T. Liu, Oxidative dehydrogenation of propane to propylene in the presence of CO₂ over gallium nitride supported on NaZSM-5, *Ind. Eng. Chem. Res.* 60 (2021) 2807–2817, <https://doi.org/10.1021/acs.iecr.0c04487>.
- [19] Z.Y. Wang, Z.H. He, Y.C. Sun, M.X. He, K. Wang, W.T. Wang, Y. Yang, J.G. Chen, Z. T. Liu, Dehydrogenation of propane in the presence of CO₂ over GaN/SiO₂ catalysts: relationship between the type of SiO₂ and the activity, *Chem. Eng. J.* 433 (2022) 134443, <https://doi.org/10.1016/j.cej.2021.134443>.
- [20] L.Y. Li, Z.Y. Wang, S.Y. Yang, J.G. Chen, Z.H. He, K. Wang, Q.X. Luo, Z.W. Liu, Z. T. Liu, Understanding the role of Fe doping in tuning the size and dispersion of GaN nanocrystallites for CO₂-assisted oxidative dehydrogenation of propane, *ACS Catal.* 12 (2022) 8527–8543, <https://doi.org/10.1021/acscatal.2c01989>.
- [21] Z.H. He, B.T. Wu, Z.Y. Wang, S.Y. Yang, K. Wang, J.J. Shi, M.X. He, W. Wang, Z. T. Liu, Photothermal catalytic CO₂ oxidative dehydrogenation of propane to propylene over BiOX (X= Cl, Br, I) nanocatalysts, *Green. Chem.* 24 (2022) 8270–8279, <https://doi.org/10.1039/D2GC02571J>.
- [22] R.Q. Miao, Z.H. He, B.T. Wu, J. Liu, S.W. Wang, K. Wang, W. Wang, L. Li, Z.T. Liu, Activated carbon-supported BiOI in CO₂ adsorption and electron transfer for photothermally catalyzed CO₂ oxidative dehydrogenation of propane, *Chem. Eng. J.* 481 (2024) 148293, <https://doi.org/10.1016/j.cej.2023.148293>.
- [23] Z.J. Zhu, Z.H. He, S.W. Wang, B.T. Wu, Y. Tian, Y.C. Sun, K. Wang, W. Wang, H. Wang, Z.T. Liu, Photothermal catalytic CO₂ oxidative dehydrogenation of propane over Co-Mn bimetallic oxides supported on MCM-41 molecular sieve, *Mol. Catal.* 559 (2024) 114070, <https://doi.org/10.1016/j.mcat.2024.114070>.
- [24] C. Liu, J. Kang, Z.Q. Huang, Y.H. Song, Y.S. Xiao, J. Song, J.X. He, C.R. Chang, H. Q. Ge, Y. Wang, Z.T. Liu, Z.W. Liu, Gallium nitride catalyzed the direct hydrogenation of carbon dioxide to dimethyl ether as primary product, *Nat. Commun.* 12 (2021) 2305, <https://doi.org/10.1038/s41467-021-22568-4>.
- [25] H. Pang, W. Zhou, H. Hu, L. Liu, J. Ye, D. Wang, Polar-surface-dominated zigzag GaN nanowires with alternate H₂ and O₂ evolution sites for photocatalytic overall water splitting, *Appl. Catal. A-Gen.* 654 (2023) 119084, <https://doi.org/10.1016/j.apcata.2023.119084>.
- [26] H.S. Jung, Y.J. Hong, Y. Li, J. Cho, Y.J. Kim, G.C. Yi, Photocatalysis using GaN nanowires, *ACS Nano* 2 (2008) 637–642, <https://doi.org/10.1021/nn700320y>.
- [27] K. Liu, B. Zhang, J. Zhang, W. Lin, J. Wang, Y. Xu, Y. Xiang, T. Hisatomi, K. Domon, G. Ma, Synthesis of narrow-band-gap GaN:ZnO solid solution for photocatalytic overall water splitting, *ACS Catal.* 12 (2022) 14637–14646, <https://doi.org/10.1021/acscatal.2c04361>.
- [28] S. Schäfer, S.A. Wyryzgol, R. Caterino, A. Jentys, S.J. Schoell, M. Hävecker, A. Knop-Gericke, J.A. Lercher, I.D. Sharp, M. Stutzmann, Platinum nanoparticles on gallium nitride surfaces: effect of semiconductor doping on nanoparticle reactivity, *J. Am. Chem. Soc.* 134 (2012) 12528–12535, <https://doi.org/10.1021/ja3020132>.
- [29] E. Grabowska, Selected perovskite oxides: characterization, preparation and photocatalytic properties—a review, *Appl. Catal. B-Environ.* 186 (2016) 97–126, <https://doi.org/10.1016/j.apcatb.2015.12.035>.
- [30] B. Moss, Q. Wang, K.T. Butler, R. Grau-Crespo, S. Selim, A. Regoutz, T. Hisatomi, R. Godin, D.J. Payne, A. Kafizas, Linking in situ charge accumulation to electronic structure in doped SrTiO₃ reveals design principles for hydrogen-evolving photocatalysts, *Nat. Mater.* 20 (2021) 511–517, <https://doi.org/10.1038/s41563-020-00868-2>.
- [31] H. Ge, Y. Kuwahara, K. Kusu, H. Kobayashi, H. Yamashita, Enhanced visible-NIR absorption and oxygen vacancy generation of Pt/H_xMoWO_y by H-spillover to facilitate photothermal catalytic CO₂ hydrogenation Yamashita, *J. Mater. Chem. A* 10 (2022) 10854–10864, <https://doi.org/10.1039/D2TA01595A>.
- [32] G. Li, M. Zhang, J. Chen, Q. Li, H. Jia, Combined effects of Pt nanoparticles and oxygen vacancies to promote photothermal catalytic degradation of toluene, *J. Hazard. Mater.* 449 (2023) 131041, <https://doi.org/10.1016/j.jhazmat.2023.131041>.
- [33] J.P. Perdew, K. Burke, M. Ernzerhof, Generalized gradient approximation made simple, *Phys. Rev. Lett.* 77 (1996) 3865, <https://doi.org/10.1103/physrevlett.77.3865>.
- [34] G. Kresse, J. Furthmüller, Efficiency of ab-initio total energy calculations for metals and semiconductors using a plane-wave basis set, *Comput. Mater. Sci.* 6 (1996) 15–50, [https://doi.org/10.1016/0927-0256\(96\)00008-0](https://doi.org/10.1016/0927-0256(96)00008-0).
- [35] P.E. Blöchl, Projector augmented-wave method, *Phys. Rev. B* 50 (1994) 17953, <https://doi.org/10.1103/PhysRevB.50.17953>.
- [36] F. Giustino, S.G. Louie, M.L. Cohen, Electron-phonon renormalization of the direct band gap of diamond, *Phys. Rev. Lett.* 105 (2010) 265501, <https://doi.org/10.1103/physrevlett.105.265501>.
- [37] L. Xiao, X. Xu, Y. Jia, G. Hu, Y. Yuan, Y. Yu, G. Zou, Pyroelectric nanoplates for reduction of CO₂ to methanol driven by temperature-variation, *Nat. Commun.* 12 (2021) 318, <https://doi.org/10.1038/s41467-021-23801-w>.
- [38] F. Fang, F. Xu, Z. Su, X. Li, W. Han, Y. Qin, J. Ye, K. Chang, Understanding targeted modulation mechanism in SrTiO₃ using K⁺ for solar water splitting, *Appl. Catal. B-Environ.* 316 (2022) 121613, <https://doi.org/10.1016/j.apcatb.2022.121613>.
- [39] Y. Qin, F. Fang, Z. Xie, H. Lin, K. Zhang, X. Yu, K. Chang, La, Al-codoped SrTiO₃ as a photocatalyst in overall water splitting: significant surface engineering effects on defect engineering, *ACS Catal.* 11 (2021) 11429–11439, <https://doi.org/10.1021/acscatal.1c02874>.
- [40] C. Lee, Y. Jeon, S. Hata, J.I. Park, R. Akiyoshi, H. Saito, Y. Teraoka, Y.G. Shul, H. Einaga, Three-dimensional arrangements of perovskite-type oxide nano-fiber webs for effective soot oxidation, *Appl. Catal. B-Environ.* 191 (2016) 157–164, <https://doi.org/10.1016/j.apcatb.2016.03.001>.
- [41] Z. Zhao, R.V. Goncalves, S.K. Barman, E.J. Willard, E. Byle, R. Perry, Z. Wu, M. N. Huda, A.J. Moulé, F.E. Osterloh, Electronic structure basis for enhanced overall water splitting photocatalysis with aluminum doped SrTiO₃ in natural sunlight, *Energ. Environ. Sci.* 12 (2019) 1385–1395, <https://doi.org/10.1039/C9EE00310J>.
- [42] X. Zhang, C. Pei, X. Chang, S. Chen, R. Liu, Z.J. Zhao, R. Mu, J. Gong, FeO₆ octahedral distortion activates lattice oxygen in perovskite ferrite for methane partial oxidation coupled with CO₂ splitting, *J. Am. Chem. Soc.* 142 (2020) 11540–11549, <https://doi.org/10.1021/jacs.0c04643>.
- [43] X. Yu, J. Wang, X. Fu, H. Meng, Y. Zhu, Y. Zhang, Construction of Z-scheme SrTiO₃/Ag/Ag₃PO₄ photocatalyst with oxygen vacancies for highly efficient degradation activity towards tetracycline, *Sep. Purif. Technol.* 241 (2020) 116718, <https://doi.org/10.1016/j.seppur.2020.116718>.
- [44] K. Xie, N. Umezawa, N. Zhang, P. Reunchan, Y. Zhang, J. Ye, Self-doped SrTiO_{3-δ} photocatalyst with enhanced activity for artificial photosynthesis under visible light, *Energ. Environ. Sci.* 4 (2011) 4211–4219, <https://doi.org/10.1039/C1EE01594J>.
- [45] W. Zhang, Y. Li, L. Wang, F. Zhang, Y. Ai, G. Shao, P. Zhang, In situ construction of Cyano-modified g-C₃N₄ nanolayer-coated SrTiO₃ nanotubes by Gas-Solid reaction for efficient photocatalytic solar fuel production, *Chem. Eng. J.* 469 (2023) 143817, <https://doi.org/10.1016/j.cej.2023.143817>.
- [46] L. Mu, Y. Zhao, A. Li, S. Wang, Z. Wang, J. Yang, Y. Wang, T. Liu, R. Chen, J. Zhu, Enhancing charge separation on high symmetry SrTiO₃ exposed with anisotropic facets for photocatalytic water splitting, *Energ. Environ. Sci.* 9 (2016) 2463–2469, <https://doi.org/10.1039/C6EE00526H>.
- [47] C.Q. Li, S.S. Yi, D.L. Chen, Y. Liu, Y.J. Li, S.Y. Lu, X.Z. Yue, Z.Y. Liu, Oxygen vacancy engineered SrTiO₃ nanofibers for enhanced photocatalytic H₂ production, *J. Mater. Chem. A* 7 (2019) 17974–17980, <https://doi.org/10.1039/C9TA03701B>.
- [48] Y. Wang, W. Zheng, F. Chen, X. Zhan, Mechanistic study of propylene oxidation over a Bi-molybdate catalyst by in situ DRIFTS and probe molecules, *Appl. Catal. A-Gen.* 351 (2008) 75–81, <https://doi.org/10.1016/j.apcata.2008.08.029>.
- [49] T. Zhang, X. Lang, A. Dong, X. Wan, S. Gao, L. Wang, L. Wang, W. Wang, Difference of oxidation mechanism between light C3–C4 alkane and alkene over mullite YMn₂O₅ oxides' catalyst, *ACS Catal.* 10 (2020) 7269–7282, <https://doi.org/10.1021/acscatal.0c00703>.
- [50] J. Dou, J. Funderburg, K. Yang, J. Liu, D. Chacko, K. Zhang, A.P. Harvey, V. P. Haribal, S.J. Zhou, F. Li, Ce_xZr_{1-x}O₂-supported CrO_x catalysts for CO₂-assisted oxidative dehydrogenation of propane—probing the active sites and strategies for enhanced stability, *ACS Catal.* 13 (2022) 213–223, <https://doi.org/10.1021/acscatal.2c05286>.
- [51] G. Li, N. Li, Y. Sun, Y. Qu, Z. Jiang, Z. Zhao, Z. Zhang, J. Cheng, Z. Hao, Efficient defect engineering in Co-Mn binary oxides for low-temperature propane oxidation, *Appl. Catal. B-Environ.* 282 (2021) 119512, <https://doi.org/10.1016/j.apcatb.2020.119512>.
- [52] B. Deng, H. Song, K. Peng, Q. Lia, J. Ye, Metal-organic framework-derived Ga-Cu/CeO₂ catalyst for highly efficient photothermal catalytic CO₂ reduction, *Appl. Catal. B-Environ.* 298 (2021) 120519, <https://doi.org/10.1016/j.apcatb.2021.120519>.

- [53] Y. Wang, S. Kattel, W. Gao, K. Li, P. Liu, J.G. Chen, H. Wang, Exploring the ternary interactions in Cu-ZnO-ZrO₂ catalysts for efficient CO₂ hydrogenation to methanol, *Nat. Commun.* 10 (2019) 1166, <https://doi.org/10.1038/s41467-019-09072-6>.
- [54] Z. Ren, Z. Wu, W. Song, W. Xiao, Y. Guo, J. Ding, S.L. Suib, P.X. Gao, Low temperature propane oxidation over Co₃O₄ based nano-array catalysts: Ni dopant effect, reaction mechanism and structural stability, *Appl. Catal. B-Environ.* 180 (2016) 150–160, <https://doi.org/10.1016/j.apcatb.2015.04.021>.
- [55] Y. Wang, C. Wöll, IR spectroscopic investigations of chemical and photochemical reactions on metal oxides: bridging the materials gap, *Chem. Soc. Rev.* 46 (2017) 1875–1932, <https://doi.org/10.1039/C6CS00914J>.
- [56] S. Bai, Q. Shao, P. Wang, Q. Dai, X. Wang, X. Huang, Highly active and selective hydrogenation of CO₂ to ethanol by ordered Pd–Cu nanoparticles, *J. Am. Chem. Soc.* 139 (2017) 6827–6830, <https://doi.org/10.1021/jacs.7b03101>.
- [57] F. Wang, S. He, H. Chen, B. Wang, L. Zheng, M. Wei, D.G. Evans, X. Duan, Active site dependent reaction mechanism over Ru/CeO₂ catalyst toward CO₂ methanation, *J. Am. Chem. Soc.* 138 (2016) 6298–6305, <https://doi.org/10.1021/jacs.6b02762>.
- [58] B. Yan, Q. Wu, J. Cen, J. Timoshenko, A.I. Frenkel, D. Su, X. Chen, J.B. Parise, E. Stach, A. Orlov, Highly active subnanometer Rh clusters derived from Rh-doped SrTiO₃ for CO₂ reduction, *Appl. Catal. B-Environ.* 237 (2018) 1003–1011, <https://doi.org/10.1016/j.apcatb.2018.06.074>.
- [59] E. Guglielminotti, Infrared study of syngas adsorption on zirconia, *Langmuir* 6 (1990) 1455–1460, <https://doi.org/10.1021/acs.jpc.3c01185>.
- [60] S. Kattel, B. Yan, Y. Yang, J.G. Chen, P. Liu, Optimizing binding energies of key intermediates for CO₂ hydrogenation to methanol over oxide-supported copper, *J. Am. Chem. Soc.* 138 (2016) 12440–12450, <https://doi.org/10.1021/jacs.6b05791>.
- [61] S. Lawsona, K. Baamrana, K. Newporta, T. Alghamadia, G. Jacobsb, F. Rezaeia, A. A. Rownaghi, Integrated direct air capture and oxidative dehydrogenation of propane with CO₂ at isothermal conditions, *Appl. Catal. B-Environ.* (303) (2022) 120907, <https://doi.org/10.1016/j.apcatb.2021.120907>.
- [62] C. Asokan, L. DeRita, P. Christopher, Using probe molecule FTIR spectroscopy to identify and characterize Pt-group metal based single atom catalysts, *Chin. J. Catal.* 38 (2017) 1473–1480, [https://doi.org/10.1016/S1872-2067\(17\)62882-1](https://doi.org/10.1016/S1872-2067(17)62882-1).